JACS
JOURNAL OF THE AMERICAN CHEMICAL SOCIETY
Article
pubs.acs.org/JACS

Influence of a Nano Phase Segregation on the Thermoelectric Properties of the p-Type Doped Stannite Compound $Cu_{2+x}Zn_{1-x}GeSe_4$

Wolfgang G. Zeier,[†,‡] Aaron LaLonde,[‡] Zachary M. Gibbs,[§] Christophe P. Heinrich,[†] Martin Panthöfer,[†] G. Jeffrey Snyder,*[,‡] and Wolfgang Tremel*[,†]

[†]Institut für Anorganische Chemie und Analytische Chemie der Johannes Gutenberg-Universität, Duesbergweg 10-14, D-55099 Mainz, Germany

[‡]Material Science and [§]Chemical Engineering, California Institute of Technology, Pasadena, California 91125, United States

ABSTRACT: Engineering nanostructure in bulk thermoelectric materials has recently been established as an effective approach to scatter phonons, reducing the phonon mean free path, without simultaneously decreasing the electron mean free path for an improvement of the performance of thermoelectric materials. Herein the synthesis, phase stability, and thermoelectric properties of the solid solutions $Cu_{2+x}Zn_{1-x}GeSe_4$ (x = 0−0.1) are reported. The substitution of Zn^{2+} with Cu^{+} introduces holes as charge carriers in the system and results in an enhancement of the thermoelectric efficiency. Nano-sized impurities formed via phase segregation at higher dopant contents have been identified and are located at the grain boundaries of the material. The impurities lead to enhanced phonon scattering, a significant reduction in lattice thermal conductivity, and therefore an increase in the thermoelectric figure of merit in these materials. This study also reveals the existence of an insulator-to-metal transition at 450 K.

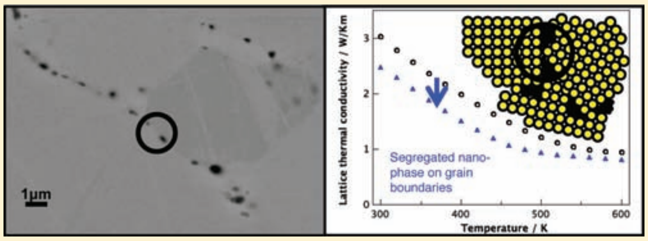

■ INTRODUCTION

Solid-state cooling and power generation based on thermoelectric effects have been the focus of recent research in the search for alternative energy technologies.[1,2] Thermoelectric devices are currently used for deep space power generation and other specialized applications, with the recovery of wasted heat as a main goal for future applications. The fact that current thermoelectric materials with high efficiencies are mainly telluride based[3−7] provides the motivation for the discovery of new compounds to be potential candidates for high-efficiency thermoelectrics.

The performance of a material is described by the thermoelectric figure of merit zT ($zT = \alpha^2 T/\rho\cdot\kappa$) at the absolute temperature T. A suitable material for thermoelectric applications must have a large Seebeck coefficient α, low resistivity ρ, and low total thermal conductivity κ. The total thermal conductivity is the sum of the lattice thermal conductivity κ_{lattice} and the electronic thermal conductivity κ_{el}. However, these transport properties are strongly coupled and the desired combination is difficult to obtain. Different strategies to yield a high figure of merit include optimization of the electronic transport by precise doping to obtain an optimum carrier concentration,[8,9] utilization of the material structure to result in a reduction of the phonon mean free path to decrease lattice thermal conductivity, e.g. in filled skutterudites,[10−12] or use of nanostructuring to reduce the phonon mean free path.[13−15]

In an attempt to broaden the quest for abundant materials with low thermal conductivities, Chen et al. have recently reported on the transport properties of quaternary tetrahedrally bonded $Cu_2(Zn/Cd)SnSe_4$.[16−18] Despite being wide band gap compounds with low electron mobility, these materials exhibit fairly good thermoelectric performance upon “doping” due to the very low intrinsic thermal conductivities,[16−19] with recent attempts to further reduce the thermal conductivity due to nano crystals.[20,21] There exists a whole family of structurally related quaternary compounds of the formula Cu_2−II−IV−$S_4(Se_4)$, with II = Mn, Fe, Co, Ni, Zn, Cd, Hg and IV = Si, Ge, Sn,[22] which have been studied for their performance as possible compounds for photovoltaic applications due to possible band gap tuning: e.g., in $Cu_2ZnSnSe_{4-x}S_x$.[23−25] The structural robustness of these compounds regarding different elements should inevitably lead to the possibility of precise doping in these materials to obtain an optimum charge carrier concentration, which in combination with the low intrinsic thermal conductivities would lead to a whole range of possible thermoelectric materials.

In order to understand and compare the published transport properties in this class of compounds, the current study focuses on the solid solution $Cu_2ZnGeSe_4$. Structurally related to sphalerite, $Cu_2ZnGeSe_4$ crystallizes in the tetragonal stannite

Received: February 13, 2012
Published: April 5, 2012

structure ($I\bar{4}2m$, $a = 5.622(0)$ Å, $c = 11.060(0)$ Å, $Z = 2$),[22] shown in Figure 1.

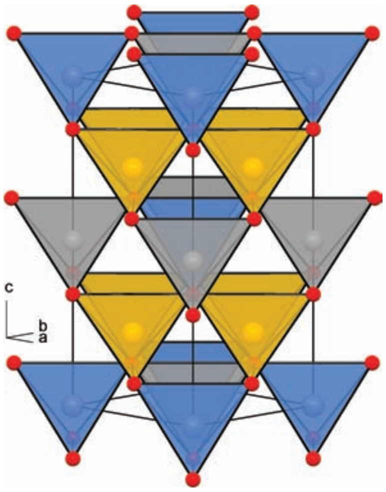

Figure 1. Crystal structure of stannite $Cu_2ZnGeSe_4$. Cu atoms are yellow, Ge atoms are gray, Zn atoms are blue, and Se atoms are red, with the tetrahedral coordination of the elements indicated.

In this work the synthesis, phase stability, and thermoelectric properties of the quaternary compound $Cu_2ZnGeSe_4$ are reported, as well as the effect of replacing Zn^{2+} with Cu^+ and an observed phase transition at 450 K, previously not reported. It is shown that substitution of Zn with Cu introduces charge carriers, resulting in a higher figure of merit zT and additionally leading to a phase segregation of nanosized $Cu_{2-\delta}Se$. This nanosized phase leads to enhanced phonon scattering and results in a significant reduction in the lattice thermal conductivity in these materials.

■ EXPERIMENTAL SECTION

Synthesis. Bulk samples of polycrystalline $Cu_{2+x}Zn_{1-x}GeSe_4$ with compositions of $x = 0$, 0.025, 0.05, 0.075, and 0.1 were prepared via solid-state reactions using elemental powders of Cu (Alfa Aesar, 99.999%), Zn (Sigma Aldrich, 99.995%), Ge (Chempur, 99.99%), and Se (Alfa Aesar, 99.999%). The phase purity of the starting materials was verified by X-ray diffraction, and all synthetic procedures were carried out in a N_2 drybox. Annealing was performed in evacuated quartz ampules, which were preheated at 1073 K under dynamic vacuum for 5 h to ensure dry conditions.

The starting elements were thoroughly ground, sealed in quartz ampules, heated to 923 K at 5 K/min, and annealed for 48 h. The ampules were cooled at 5 K/min, and the obtained materials were ground, sealed in quartz ampules again, and then reannealed at 1073 K for 96 h with the aforementioned heating and cooling rates. It was found that the second annealing step was necessary to prevent the formation of the binary and ternary compositions. The quartz ampules were 10−12 cm in length and 11 mm inner diameter with a maximum amount of 1.5 g of starting materials within the ampule. This ampule geometry was found to prevent significant loss of selenium at higher temperatures, indicated by red selenium precipitation present on longer ampules. The obtained powders were hand ground and consolidated into 1−1.5 mm thick, 12 mm diameter disks at 873 K for 5 h under a pressure of 40 MPa by induction hot pressing in high-density graphite dies.[26] The resulting samples have more than 97% theoretical density.

Physical Characterization. X-ray diffraction measurements were performed on a Siemens D5000 powder diffractometer with a Braun M50 position-sensitive detector and Cu Kα_1 radiation (Ge(220) monochromator) with a step size of 0.0078°. Rietveld refinements were performed with TOPAS Academic V4.1[27] applying the fundamental parameter approach using the crystallographic data from Schäfer and Nitsche.[22] Scanning electron microscopy (SEM) images and energy-dispersive X-ray spectroscopy (EDS) of the consolidated materials were taken using a Zeiss 1550 VP SEM in the quadrant backscattering detector (QBSD) and the secondary electron detector (SE2) mode. Optical absorption spectra of the roughened consolidated disks were measured at room temperature by a Cary 5000 UV−visible−near-IR spectrometer equipped with an integrating sphere. Absorption coefficients were calculated from the diffuse reflectance using the Kubelka−Munk function.

Combined thermogravimetric analysis (TGA) and differential scanning calorimetry (DSC) were performed using a Netzsch STA 449 instrument. Thermal diffusivity was measured using a Netzsch laser flash diffusivity instrument (LFA 457); samples were coated with a thin layer of graphite to minimize errors in the emissivity. The data were analyzed using a Cowan model with pulse correction. Heat capacity (C_p) was estimated using the method of Dulong-Petit ($C_p = 3R$, k_B per atom), and theoretical densities were calculated from the molar mass and the lattice parameters for each composition obtained from X-ray diffraction. The Seebeck coefficient was calculated from the slope of the thermopower vs temperature gradient measurements from chromel−Nb thermocouples.[28] Electrical resistivity, Hall coefficient, and carrier concentration were measured using the Van der Pauw technique under a reversible magnetic field of 2 T and pressure-assisted contacts. All measurements were performed under dynamic vacuum and on multiple samples for each composition. Shown measurement data represent both heating and cooling data. The combined uncertainty for all measurements involved in zT determination is 20%.

■ RESULTS AND DISCUSSION

Chemical Characterization. All samples were checked for phase purity prior to any transport measurements, and selected powder diffraction data are shown in Figure 3 for each composition. In all compositions with $x < 0.075$ all reflections can be indexed to $Cu_2ZnGeSe_4$ and no secondary phase is observed. However, the samples with the nominal composition of $Cu_{2.1}Zn_{0.9}GeSe_4$ show an impurity phase of $Cu_{2-\delta}Se$ with a weight percentage of 1−2% indicated by Rietveld refinement. Lattice parameters were refined, and no significant change was observed upon doping Zn^{2+} with Cu^+, due to the relatively similar ionic radii of the species. Rietveld refinements of powder samples prior to the hot-pressing procedure and data taken from consolidated samples do not show any significant texture in this material. We therefore believe that disks of this polycrystalline material are suitable for a thermoelectric characterization.

Combined TGA/DSC analysis of the material from ambient temperature to 1100 K revealed a slightly exothermic effect around 450 K corresponding to a phase transition (Figure 2), which has not been reported previously.[29,30]

At present, the nature of this phase transformation remains unclear and a detailed structural investigation and analysis is necessary. Significant weight loss does not occur until 973 K, while purged with argon; however, measurements under dynamic vacuum lead to a significant evaporation of selenium above 723 K. Therefore, all measurements were performed up to 673 K to ensure the thermal stability of the samples.

At room temperature the optical data in Figure 3c plotted as $(\alpha h\nu)^2$ against photon energy, where α is the absorption coefficient, h the Planck constant, and ν the wavenumber, give an estimated optical band gap E_g of 1.4 eV, which is consistent with the reported data of this class of wide band gap materials.[29]

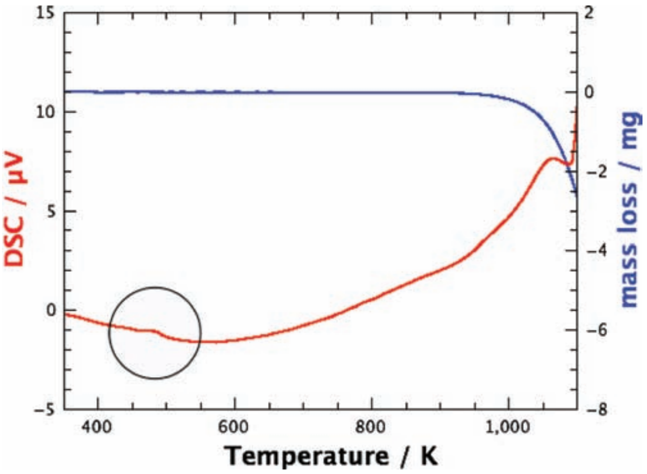

Figure 2. TGA/DSC data for $Cu_2ZnGeSe_4$, with the slightly exothermic effect (black circle) indicating a phase transition.

Scanning electron microscopy of polished and fractured surfaces showed very high densities of the samples, in agreement with the high density values measured after hot pressing. Selected SEM micrographs of polished surfaces for different doping contents are shown in Figure 4. SEM micrographs are shown in backscattered (QBSD) and secondary electron mode (SE2) to distinguish among impurities, voids, and the residue of polishing particles. Energy-dispersive X-ray spectroscopy was utilized to verify the stoichiometry.

Contrasts in the micrographs are due to different orientations of the grains of the compound $Cu_{2+x}Zn_{1-x}GeSe_4$, and grain sizes are between 10 and 20 μm. Scanning electron microscopy at higher magnifications revealed impurity phases present in the material that were undetected by X-ray diffraction. The impurity phase is attributed to a segregation triggered by higher contents of Cu. Samples with the nominal composition of $Cu_{2.05}Zn_{0.95}GeSe_4$ show the two impurity phases CuSe and $Cu_{2-\delta}Se$ as white and black spots, respectively. However, higher Cu contents mainly lead to the formation of $Cu_{2-\delta}Se$ for $x = 0.075$ and $x = 0.1$, which is in accordance with the X-ray diffraction data for $x = 0.1$ (Figure 3). This phase segregation is possibly a result of a charge imbalance in the material. Substitution of Zn^{2+} with Cu^+ leads to the formation of holes, or Se^- (for localized charges). For higher doping levels the excess of Cu leads to a phase segregation to form the energetically more stable species Se^{2-} in the secondary phase. It is possible that, above a certain amount of excess Cu, all the extra Cu segregates in the form of $Cu_{2-\delta}Se$. The amount of the impurity phase should then be proportional to the amount of extra Cu. These impurities have grain sizes of 250 nm and smaller and are mainly located at the grain boundaries.

Electronic Transport Properties. The temperature dependence of the resistivity for different doping concentrations in $Cu_{2+x}Zn_{1-x}GeSe_4$ is shown in Figure 5. As expected for a wide band gap semiconductor,[31] unsubstituted $Cu_2ZnGeSe_4$ exhibits a high electrical resistivity at room temperature and decreases with increasing temperature. The aforementioned phase transformation at around 450 K has a significant impact on the electrical resistivity, leading to an increase in resistivity with temperature for all doping levels, similar to metallic transport behavior, and the temperature of the transition seems to be composition dependent. Thus, this transition can be considered an insulator-to-metal transition.

While substitution introduces charge carriers and results in a decrease of the resistivity over orders of magnitude, the change in the resistivity does not entirely follow the trend expected for the substitution with Cu^{2+} for Zn^+. The exception to the expected behavior is seen at the substitution level of $x = 0.05$, which shows a lower resistivity than $x = 0.075$ and $x = 0.1$. This can be explained by the charge carrier concentrations (Figure 5) that result for each doping level, where a higher than expected carrier concentration was observed for the $x = 0.05$ sample. Expected carrier concentrations from simple charge

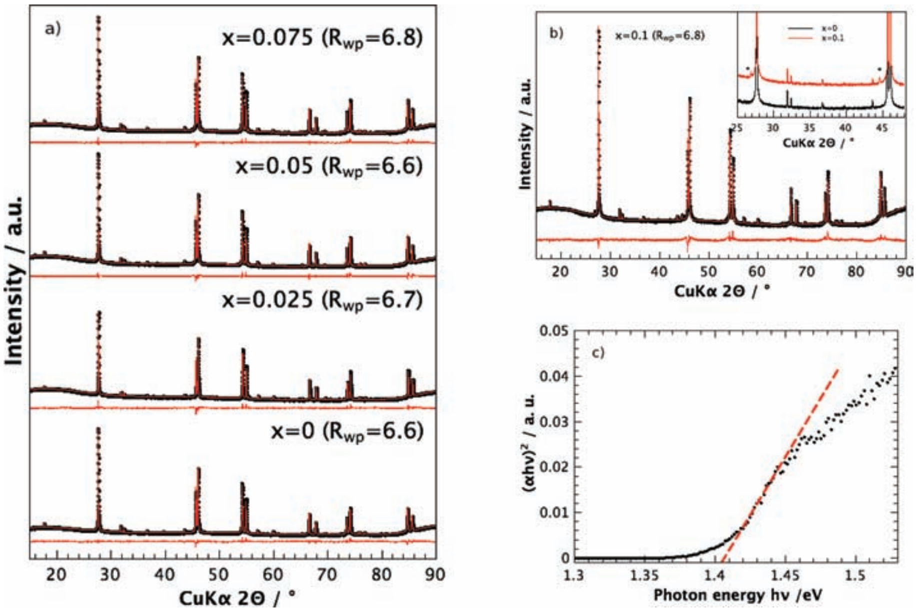

Figure 3. (a, b) Powder diffraction data for $Cu_{2+x}Zn_{1-x}GeSe_4$ including profile fit, profile difference, and profile residuals from the corresponding Rietveld refinement. The intensities are plotted as the square root to show low-intensity reflections as well. The inset in (b) shows extra reflections indexed to $Cu_{2-\delta}Se$. (c) Absorption spectrum of $Cu_2ZnGeSe_4$ with the band gap extrapolation indicated.

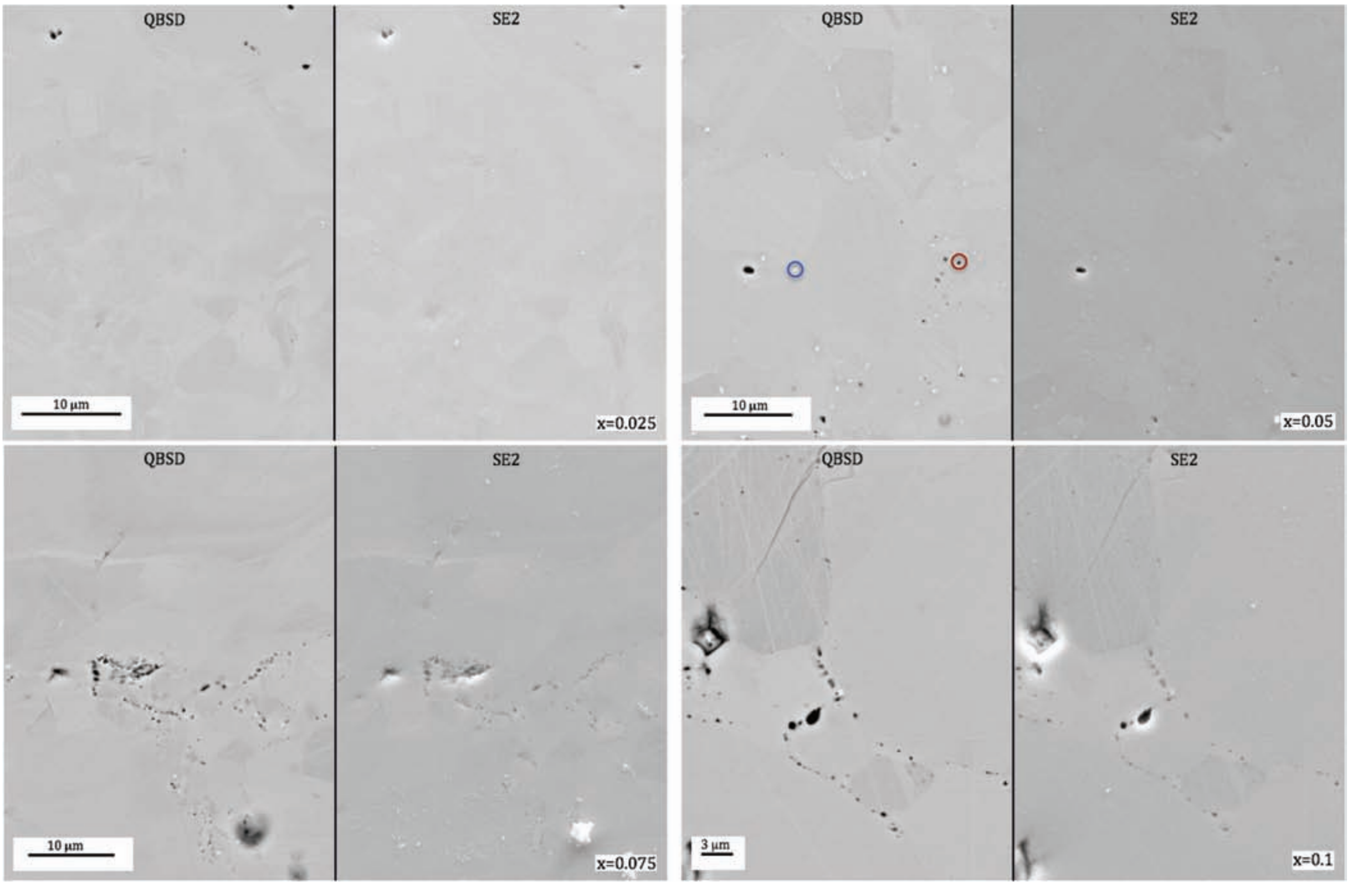

Figure 4. Scanning electron micrographs of polished surfaces for different doping contents x in $Cu_{2+x}Zn_{1-x}GeSe_4$ in backscattered (QBSD) and secondary electron mode (SE2). White spots (blue circle) and black spots (red circle) in samples with $x = 0.05$ reveal minor impurities of CuSe and $Cu_{2-\delta}Se$, respectively. Doping contents of $x = 0.075$ and $x = 0.1$ mainly show impurities of $Cu_{2-\delta}Se$ with sizes of 250 nm and smaller, mainly located at the grain boundaries.

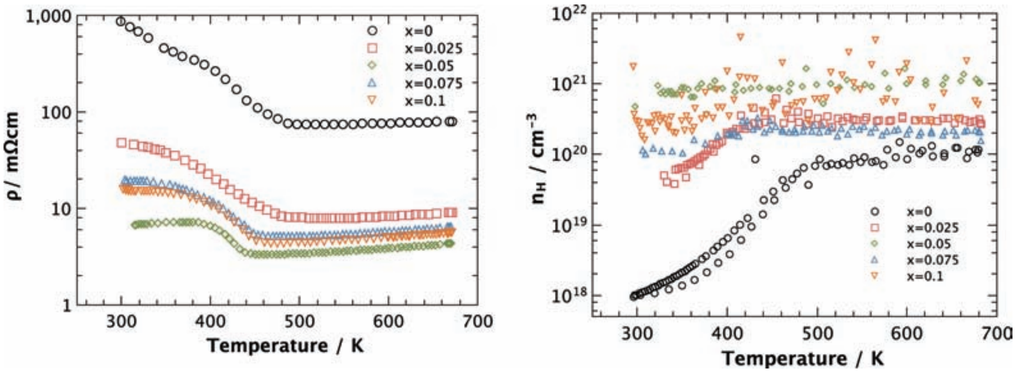

Figure 5. Resistivity ρ (left) and Hall carrier concentrations n_H (right) of $Cu_{2+x}Zn_{1-x}GeSe_4$ as a function of temperature.

counting and measured Hall carrier concentrations are shown in Figure 6. At a doping level of $x = 0.025$ the substitution has the expected effect on the carrier concentration; however, higher substitution levels deviate significantly from the charge carrier concentrations expected from simple charge counting. This behavior is attributed to the secondary phases in the material seen in the scanning electron micrographs (Figure 4). The formation of $Cu_{2-\delta}Se$ reduces the amount of Se^{2-} and Cu^+ in the matrix. Considering the case where only Se is removed from the matrix, there would be electrons left behind in the matrix which would lead to fewer holes in the material, as compared to those expected from charge counting for each level of substitution x. In the case where only Cu is removed from the matrix, the result would be more holes left behind in the matrix. In the case of phase segregation where stoichiometric Cu_2Se is formed, the individual effects of less Se and Cu in the matrix would cancel each other out and would not impact the carrier density. However, the formation of nonstoichiometric $Cu_{2-\delta}Se$ means that more Se than Cu is removed from the matrix and the overall result is fewer holes in the matrix as compared to the expected number from simple charge counting, the effect of which is shown by the measured Hall carrier concentrations shown in Figure 6. Additionally, it is likely that CuSe forms for $x = 0.05$ due to a slight excess of Se

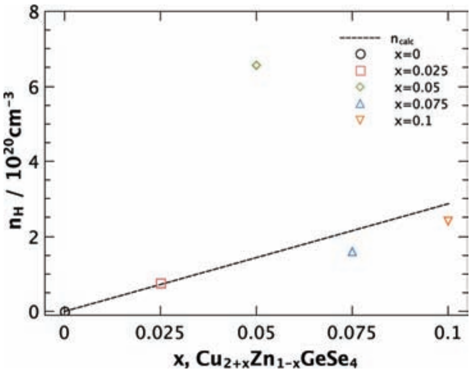

Figure 6. Expected charge carrier concentrations n_{calc} and measured Hall carrier concentrations n_H for $Cu_{2+x}Zn_{1-x}GeSe_4$.

and reduces the amount of Cu and therefore leads to more holes in the matrix.

It should be noted that measured Hall mobilities at room temperature are around 2−3 $cm^2/(V\ s)$ and are not affected by this unexpected trend, leading to the assumption that the charge carrier concentration mainly dominates the electronic transport. The Hall voltage is positive, which is expected for p-type charge carriers (holes), and the mobilities are low for a semiconductor but high for localized charges in a very ionic environment.

Figure 7 illustrates the effect of the charge carrier concentrations on the thermopower. The Seebeck coefficients are large and positive, indicating holes as the majority carrier type, consistent with the carrier concentration and Hall mobilities acquired via Hall measurements. The increase of the Seebeck coefficient with increasing temperature reveals that the maximum of the thermopower is not yet reached at 670 K, which is consistent with the measured wide band gap of 1.4 eV in this material (Figure 3c). Within this measurement range, thermally activated electrons do not cause a reduction in the thermovoltage. Solutions to the Boltzmann transport equation within the relaxation time approximation have been used to model the relationship between carrier concentration and the Seebeck coefficient. The thermopower of a material can be described using the reduced chemical potential η, with the Boltzmann constant k_B and the electron charge e:[32−34]

$$\alpha = \frac{k_B}{e}\left(\frac{(2+\lambda)F_{1+\lambda}(\eta)}{(1+\lambda)F_{\lambda}(\eta)} - \eta\right) \tag{1}$$

The Fermi integrals are given by

$$F_j(\eta) = \int_0^\infty \frac{\xi^j d\xi}{1+\exp(\xi-\eta)} \tag{2}$$

with the reduced carrier energy ξ. The scattering parameter λ relates to the energy dependence of the carrier relaxation time τ, with $\tau = \tau_0 e^{\lambda-1/2}$.[35]

In this model it is assumed that only one type of carrier is present in a single parabolic band, with the assumption of acoustic phonon scattering ($\lambda = 0$). The effective mass m^* of 1.2 m_e, which was used to calculate the Pisarenko relation (Figure 7) at 360 K, was calculated from the experimental Seebeck coefficient and Hall carrier concentration for $x = 0.025$ with the carrier concentration described as[36]

$$n = 4\pi\left(\frac{2m^* k_B T}{h^2}\right)^{3/2} F_{1/2}(\eta) \tag{3}$$

Because the experimental data fall on or near the generated curve, it may be assumed that a heavily doped, single parabolic band is a good starting model for electronic transport of this system below the transition temperature. Substitution with Cu does not significantly change the effective mass or mobility of the holes and therefore confirms that the electronic transport is mainly governed by the charge carrier densities. This furthermore shows that the carrier mobility is not affected by nanoparticles of this length scale, which is expected, since the mean free paths of electrons and holes are much shorter than those of phonons.[37]

Thermal Transport Properties. The thermal diffusivity of the material was measured up to 670 K. The total thermal conductivity was calculated using $\kappa = D\rho C_p$, where D = thermal diffusivity, ρ = geometric density, and C_p = specific heat capacity. Here, use of the Dulong−Petit approximation for the heat capacity (C_p = 0.34 J g^{1-} K^{-1}) is likely to result in an underestimation (~10%) of the thermal conductivity at high temperatures.[38] The temperature dependence of the total thermal conductivity is shown in Figure 8, and the effect of the previously mentioned phase transformation can be seen at around 450 K. The thermal diffusivity is additionally shown in Figure 8.

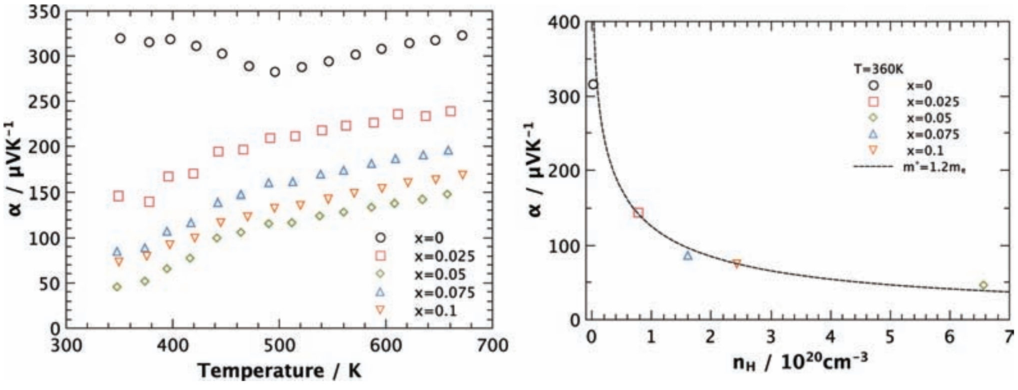

Figure 7. Seebeck coefficients α vs temperature (left) of $Cu_{2+x}Zn_{1-x}GeSe_4$, showing the phase transition in the undoped sample and experimental Seebeck coefficients as a function of Hall carrier concentration n_H (right) at 360 K. The dotted line was generated using a single parabolic band approximation and an effective mass of 1.2 m_e.

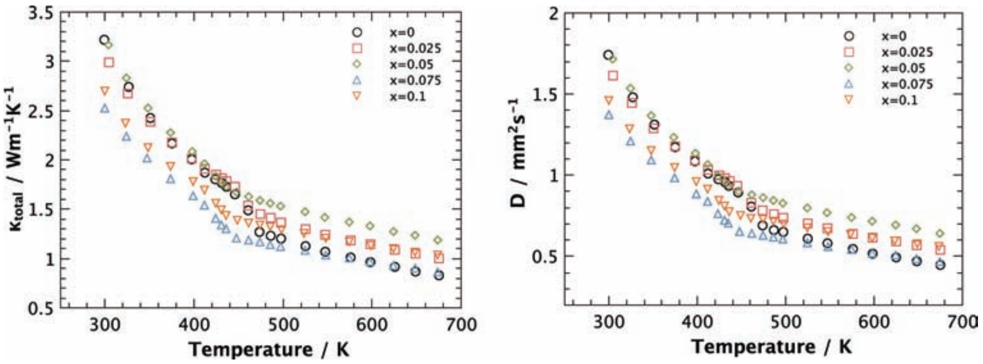

Figure 8. Total thermal conductivity κ (left) and thermal diffusivity D (right) of $Cu_{2+x}Zn_{1-x}GeSe_4$ as a function of temperature.

The total thermal conductivity of a semiconducting material is a combination of lattice, electronic, and bipolar contributions ($\kappa_{total} = \kappa_{lattice} + \kappa_{el} + \kappa_{bipolar}$). The Wiedeman−Franz relation ($\kappa_{el} = LT/\rho$) was employed to estimate the κ_{el} contribution to the thermal conductivity. Temperature-dependent Lorenz numbers (L) were calculated within the single parabolic band approximation using eq 4[33] under the assumption of acoustic

$$L = \frac{{k_B}^2}{e^2}\frac{(1+\lambda)(3+\lambda)F_{\lambda}(\eta)F_{\lambda+2}(\eta) - (2+\lambda)^2 {F_{\lambda+1}}^2(\eta)}{(1+\lambda)^2 {F_{\lambda}}^2(\eta)} \qquad (4)$$

phonon scattering ($\lambda = 0$). The reduced chemical potential η was calculated from the experimental Seebeck coefficients via eq 1.

The electronic contribution to the total thermal conductivity (Figure 9) of the undoped sample is very low, due to the high resistivity, and increases with increasing carrier concentration. The phase transformation can be seen as well, due to the change in the resistivity at the transition temperature in this material. The calculated Lorenz numbers are considerably lower than the value for the free electron model of 2.44 W Ω K^{-2}.

Subtraction of κ_{el} from κ_{total} leaves the lattice and bipolar contribution of the thermal conductivity (Figure 10). As expected for this wide band gap semiconductor, there is no evidence of a significant bipolar contribution to the total thermal conductivity in this temperature range, which would be visible as an upturn in the data at higher temperatures, and the resulting thermal conductivity is hereafter referred to as lattice thermal conductivity.

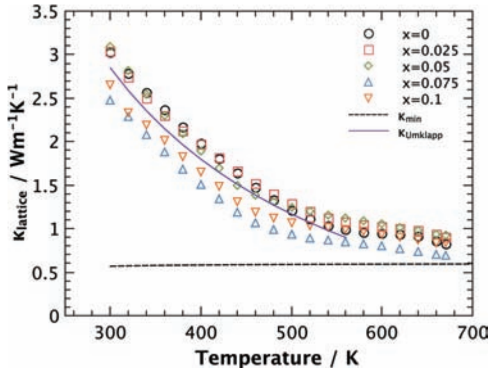

Figure 10. Temperature dependence of the lattice thermal conductivity $\kappa_{lattice}$ of $Cu_{2+x}Zn_{1-x}GeSe_4$. $\kappa_{lattice}$ exhibits a $1/T$ temperature dependence (purple line) attributed with phonon−phonon Umklapp scattering, slowly approaching the glassy limit κ_{min} (dashed line) at higher temperatures.

The lattice thermal conductivities of $Cu_{2+x}Zn_{1-x}GeSe_4$ with x = 0, 0.025, and 0.05 are the same within the range of the measurement uncertainty for the laser flash diffusivity measurements of 3%. This can be expected, since the mass contrast between Cu and Zn is low and therefore point defect scattering, due to the mass disorder, can be assumed to be negligible. The temperature dependence of $\kappa_{lattice}$ is well described by a $1/T$ dependence attributed to phonon−phonon Umklapp scatter-

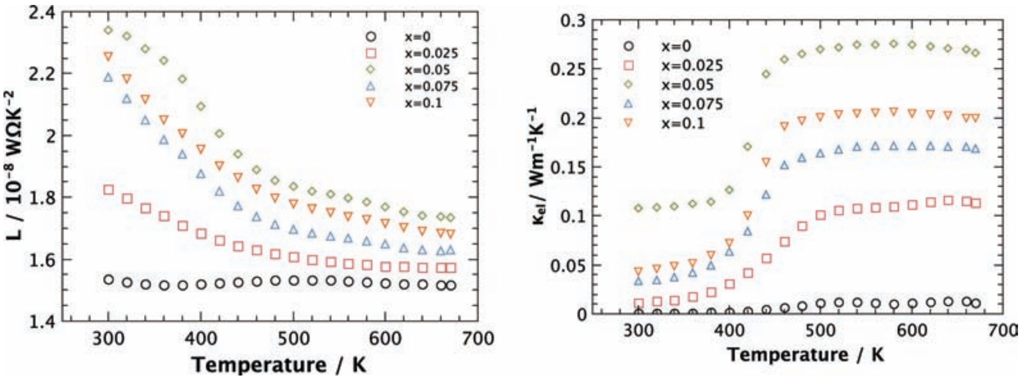

Figure 9. Calculated temperature-dependent Lorenz number L (left) and electronic thermal conductivity κ_{el} (right) of $Cu_{2+x}Zn_{1-x}GeSe_4$. Lorenz numbers are smaller than the value for the free electron model of 2.44 W Ω K^{-2}.

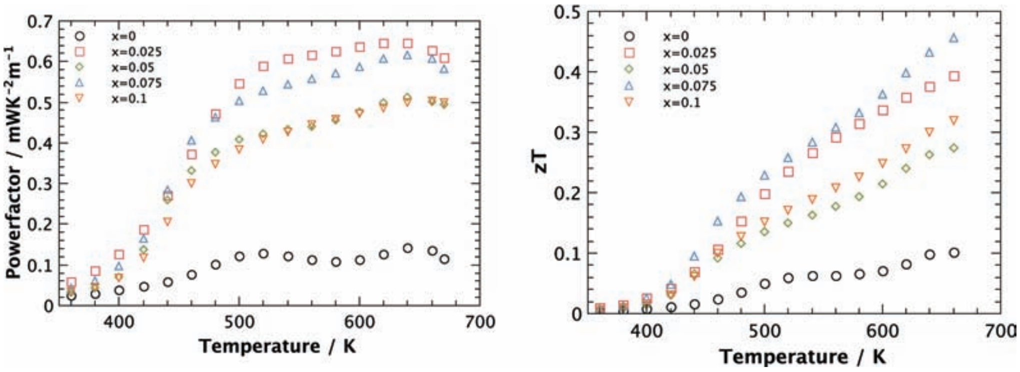

Figure 11. Temperature dependence of the power factor *PF* (left) and figure of merit *zT* (right) for the solid solutions $Cu_{2+x}Zn_{1-x}GeSe_4$. The highest power factor is achieved for the carrier concentration at the doping level of $x = 0.025$, but the highest figure of merit is for $x = 0.075$ due to the reduction of lattice thermal conductivity by nano-sized impurities.

ing, which, in materials with low mass contrast and simple crystal structures, is given by[39]

$$\kappa_{\mathrm{Umklapp}} = \frac{(6\pi^2)^{2/3}}{4\pi^2}\frac{M{v_{\mathrm{m}}}^3}{TV^{2/3}\gamma^2} \qquad (5)$$

where M is the average mass, v_{m} the average speed of sound, V the volume per atom, and γ the Grüneisen parameter.

Room-temperature ultrasonic measurements of undoped $Cu_2ZnGeSe_4$ yield the longitudinal v_{l} and transverse v_{t} speeds of sound of 4101 and 2154 m/s, respectively. The average speed of sound and the Debye temperature Θ_{D} of the material of 2409 m/s and 257 K, respectively, can be calculated via eqs 6 and 7.[40]

$$v_{\mathrm{m}} = \frac{3}{{v_{\mathrm{l}}}^{-3} + 2{v_{\mathrm{t}}}^{-3}} \qquad (6)$$

$$\Theta_{\mathrm{D}} = \frac{v_{\mathrm{m}}\hbar}{k_{\mathrm{B}}}\left(\frac{6\pi^2}{V}\right)^{1/3} \qquad (7)$$

Using eq 5 and the experimental data of the temperature-dependent lattice thermal conductivity, a Grüneisen parameter of $\gamma = 0.8$ has been determined for $Cu_2ZnGeSe_4$. This value is reasonable as compared with the room-temperature Grüneisen parameter of ZnSe of 0.8,[41] due to similar crystal structures and bonding interactions.

The assumption of a minimum scattering length for phonons as a function of the phonon frequencies leads to a model of the glassy limit of the lattice thermal conductivity, initially described by Cahill et al.[42] and recently employed to calculate the lower bound for lattice thermal conductivities κ_{min} in thermoelectric materials by Toberer et al.[43] The temperature dependence of κ_{min} is given in Figure 10. The high-temperature estimation of κ_{min} with an average volume V per atom is given by[44]

$$\kappa_{\mathrm{min}} = \frac{1}{2}\left(\frac{\pi}{6}\right)^{1/3} k_{\mathrm{B}}V^{-2/3}(2v_{\mathrm{t}} + v_{\mathrm{l}}) \qquad (8)$$

In this material, a statistically significant reduction in the lattice thermal conductivity can be seen for $x = 0.075$ and 0.1, which can be attributed to the secondary phases at these substitution levels. The nanometer scale impurities are mainly located at the grain boundaries, leading to an enhanced phonon scattering and therefore a significant reduction in phonon mean free path. The effect of the reduction leads to a lowering in lattice thermal conductivity of 0.3–0.5 W m^{-1} K^{-1} at room temperature, with $\kappa_{\mathrm{lattice}}$ approaching the minimum value of 0.6 Wm^{1-}K^{-1} at higher temperatures.

Figure of Merit. The power factor $PF = \alpha^2/\rho$ and figure of merit $zT = \alpha^2 T/\rho{\cdot}\kappa$ are shown in Figure 11. The carrier concentration of 7.7×10^{19} cm^{-3} of $x = 0.025$ leads to the highest power factor in the material, while higher doping levels introduce too many charge carriers. However, the figure of merit of the samples with $x = 0.075$ are higher than those with $x = 0.025$, due to a statistically significant reduction of the lattice thermal conductivity induced by the nano-sized impurities located at the grain boundaries. The material exhibits the highest figure of merit of 0.45 at 670 K for $x = 0.075$. The maximum zT is not yet reached in this temperature range, because the wide band gap of these compounds effectively suppresses the thermal activation of minority charge carriers. Additionally, the incorporation of a protective coating to prevent the evaporation of selenium will stabilize the material for use and measurement at higher temperatures that should result in higher figure of merit values as seen for $Cu_2ZnSnSe_4$[16,18] (zT = 0.45 at 700 K and 0.9 at 860 K).

CONCLUSION

Inspired by the thermoelectric properties of the quaternary tetrahedrally bonded $Cu_2(Zn/Cd)SnSe_4$, we investigated the thermoelectric properties of the solid solutions $Cu_{2+x}Zn_{1-x}GeSe_4$. A phase transition at 450 K has been identified, and it has an influence on the transport properties in this material, leading to an insulator-to-metal transition. Substitution of Zn^{2+} with Cu^+ introduces holes as charge carriers but also leads to the formation of impurities by phase segregation which greatly influence the charge carrier concentration. These nanometer-sized impurities are primarily located at the grain boundaries, causing a reduction of the lattice thermal conductivity and increasing the figure of merit to 0.45 at 670 K.

AUTHOR INFORMATION

Corresponding Author

*jsnyder@caltech.edu; tremel@uni-mainz.de

Notes

The authors declare no competing financial interest.

■ ACKNOWLEDGMENTS

W.G.Z. thanks the Carl-Zeiss foundation and the Graduate School of Excellence MAINZ, funded by the State of Rhineland-Palatinate. We also acknowledge Alex Zevalkink for performing high-temperature Hall measurements at the Jet Propulsion Laboratory and Nick Heinz for obtaining EDS data and SEM micrographs.

■ REFERENCES

(1) Bell, L. E. *Science* **2008**, *321*, 1457−1461.

(2) DiSalvo, F. J. *Science* **1999**, *285*, 703−706.

(3) LaLonde, A. D.; Pei, Y.; Snyder, G. J. *Energy Environ. Sci.* **2011**, *4*, 2090.

(4) Pei, Y.; Shi, X.; LaLonde, A.; Wang, H.; Chen, L.; Snyder, G. J. *Nature* **2011**, *473*, 66−69.

(5) Hsu, K. F.; Loo, S.; Guo, F.; Chen, W.; Dyck, J. S.; Uher, C.; Hogan, T.; Polychroniadis, E. K.; Kanatzidis, M. G. *Science* **2004**, *303*, 818−821.

(6) Chung, D.; Hogan, T.; Brazis, P.; Rocci-Lane, M.; Kannewurf, C.; Bastea, M.; Uher, C.; Kanatzidis, M. G. *Science* **2000**, *287*, 1024−1027.

(7) Sootsman, J. R.; Chung, D. Y.; Kanatzidis, M. G. *Angew. Chem., Int. Ed.* **2009**, *48*, 8616−8639.

(8) Snyder, G. J.; Toberer, E. S. *Nat. Mater.* **2008**, *7*, 105−114.

(9) Toberer, E. S.; May, A. F.; Snyder, G. J. *Chem. Mater.* **2010**, *22*, 624−634.

(10) Sales, B.; Mandrus, D.; Williams, R. *Science* **1996**, *272*, 1325−1328.

(11) Nolas, G. S.; Poon, J.; Kanatzidis, M. G. *MRS Bull.* **2006**, *31*, 199−205.

(12) Shi, X.; Yang, J.; Salvador, J. R.; Chi, M.; Cho, J. Y.; Wang, H.; Bai, S.; Yang, J.; Zhang, W.; Chen, L. *J. Am. Chem. Soc.* **2011**, *133*, 7837−7846.

(13) Johnsen, S.; He, J.; Androulakis, J.; Dravid, V. P.; Todorov, I.; Chung, D. Y.; Kanatzidis, M. G. *J. Am. Chem. Soc.* **2011**, *133*, 3460−3470.

(14) Minnich, A. J.; Dresselhaus, M. S.; Ren, Z. F.; Chen, G. *Energy Environ. Sci.* **2009**, *2*, 466−479.

(15) Poudeu, P. F. P.; D'Angelo, J.; Downey, A. D.; Short, J. L.; Hogan, T. P.; Kanatzidis, M. G. *Angew. Chem., Int. Ed.* **2006**, *45*, 3835−3839.

(16) Shi, X. Y.; Huang, F. Q.; Liu, M. L.; Chen, L. D. *Appl. Phys. Lett.* **2009**, *94*, 122103.

(17) Liu, M.-L.; Chen, I.-W.; Huang, F.-Q.; Chen, L.-D. *Adv. Mater.* **2009**, *21*, 3808−3812.

(18) Liu, M.-L.; Huang, F.-Q.; Chen, L.-D.; Chen, I.-W. *Appl. Phys. Lett.* **2009**, *94*, 202103.

(19) Sevik, C. *Appl. Phys. Lett.* **2009**, *95*, 112105.

(20) Ibáñez, M.; Cadavid, D.; Zamani, R.; Garca-Castello, N.; Izquierdo-Roca, V.; Li, W.; Fairbrother, A.; Prades, J. D.; Shavel, A.; Arbiol, J.; Perez-Rodriguez, A.; Morante, J. R.; Cabot, A. *Chem. Mater.* **2012**, *24*, 562−570.

(21) Ibáñez, M.; Zamani, R.; LaLonde, A.; Cadavid, D.; Li, W.; Shavel, A.; Arbiol, J.; Morante, J. R.; Gorsse, S.; Snyder, G. J.; Cabot, A. *J. Am. Chem. Soc.* **2012**, *134*, 4060−4063.

(22) Schäfer, W.; Nitsche, R. *MRS Bull.* **1974**, *9*, 645−654.

(23) Tanaka, K.; Fukui, Y.; Moritake, N.; Uchiki, H. *Sol. Energy Mater. Sol. Cells* **2010**, *95*, 838−842.

(24) Wang, K.; Shin, B.; Reuter, K. B.; Todorov, T.; Mitzi, D. B.; Guha, S. *Appl. Phys. Lett.* **2011**, *98*, 051912.

(25) Wei, H.; Ye, Z.; Li, M.; Su, Y.; Yang, Z.; Zhang, Y. *Cryst. Eng. Commun.* **2011**, *13*, 2222.

(26) LaLonde, A. D.; Ikeda, T.; Snyder, G. J. *Rev. Sci. Instrum.* **2011**, *82*, 025104.

(27) Cohelo, A. *TOPAS Academic V4.1*, 2004.

(28) Iwanaga, S.; Toberer, E. S.; LaLonde, A.; Snyder, G. J. *Rev. Sci. Instrum.* **2011**, *82*, 063905.

(29) Matsushita, H.; Maeda, T.; Katsui, A.; Takizawa, T. *J. Cryst. Growth* **2000**, *208*, 416−422.

(30) Matsushita, H.; Ichikawa, T.; Katsui, A. *J. Mater. Sci.* **2005**, *40*, 2003−2005.

(31) Schleich, D. M.; Wold, A. *MRS Bull.* **1977**, *12*, 111−114.

(32) May, A. F.; Fleurial, J.-P.; Snyder, G. *Phys. Rev. B* **2008**, *78*, 125205.

(33) May, A. F.; Toberer, E. S.; Saramat, A.; Snyder, G. J. *Phys. Rev. B* **2009**, *80*, 125205.

(34) Zevalkink, A.; Toberer, E. S.; Zeier, W. G.; Flage-Larsen, E.; Snyder, G. J. *Energy Environ. Sci.* **2011**, *4*, 510.

(35) Goldsmid, H. J. *Applications of Thermoelectricity*; Butler & Tanner: London, 1960.

(36) Ioffe, A. F. *Semiconductor Thermoelements and Thermoelectric Cooling*; Infosearch: London, 1957.

(37) Zebarjadi, M.; Esfarjani, K.; Dresselhaus, M. S.; Ren, Z. F.; Chen, G. *Energy Environ. Sci.* **2012**, *5*, 5147.

(38) Delaire, O.; May, A. F.; McGuire, M. A.; Porter, W. D.; Lucas, M. S.; Stone, M. B.; Abernathy, D. L.; Ravi, V. A.; Firdosy, S. A.; Snyder, G. J. *Phys. Rev. B* **2009**, *80*, 184302.

(39) Toberer, E. S.; Zevalkink, A.; Snyder, G. J. *J. Mater. Chem.* **2011**, *21*, 15843−15852.

(40) Drabble, J. R.; Goldsmid, H. J. *Thermal Conduction in Semiconductors*; Pergamon Press: New York, 1961.

(41) Soma, T. *Solid State Commun.* **1980**, *34*, 927−932.

(42) Cahill, D.; Watson, S.; Pohl, R. *Phys. Rev. B* **1992**, *46*, 6131−6140.

(43) Toberer, E. S.; Zevalkink, A.; Crisosto, N.; Snyder, G. J. *Adv. Funct. Mater.* **2010**, *20*, 4375−4380.

(44) May, A. F.; Snyder, G. J. In *Thermoelectrics Handbook: Thermoelectrics and its Energy Harvesting*; Rowe, D. M., Ed.; CRC Press: Boca Raton, FL, 2012; Chapter 11.